

Surface-Phonon-Induced Rotational Dissipation for Nanoscale Solid-State Gears

H.-H. Lin^{1,*}, A. Croy¹, R. Gutierrez¹, and G. Cuniberti^{1,2,3,†}

¹*Institute for Materials Science and Max Bergmann Center of Biomaterials, TU Dresden, Dresden 01069, Germany*

²*Dresden Center for Computational Materials Science, TU Dresden, Dresden 01062, Germany*

³*Center for Advancing Electronics Dresden, TU Dresden, Dresden 01062, Germany*



(Received 10 September 2020; revised 28 November 2020; accepted 25 January 2021; published 22 February 2021)

Compared to nanoscale friction of translational motion, the mechanisms of rotational friction have received less attention. Such motion becomes an important issue for the miniaturization of mechanical machinery that often involves rotating gears. In this study, molecular-dynamics simulations are performed to explore rotational friction for solid-state gears rotating on top of different substrates. In each case, viscous damping of the rotational motion is observed and found to be induced by the pure van der Waals interaction between the gear and the substrate. The influence of different gear sizes and various substrate materials is investigated. Furthermore, the rigidities of the gear and the substrate are found to give rise to different dissipation channels. Finally, it is shown that the dominant contribution to the dissipation is related to the excitation of low-frequency surface phonons in the substrate.

DOI: [10.1103/PhysRevApplied.15.024053](https://doi.org/10.1103/PhysRevApplied.15.024053)

I. INTRODUCTION

Friction on the nanoscale is a topical subject of great interest from both a practical as well as a fundamental point of view. However, the extrapolation of well-known laws from the macroscopic domain to nanoscale friction phenomena is not straightforward and, often, the observations in this regime are in contrast to macroscopic behavior. Thus, it has been found that Amontons' law and Coulomb's law cannot be directly applied to nanoscale frictional processes [1]. Consequently, in the context of nanotribology, sliding friction has been extensively studied from different perspectives [1–6], including numerical studies of different phenomenological models [7–9] as well as various experimental techniques [10–16].

Prototypical investigations involve nanoparticles moving on a surface and interacting with it via van der Waals forces [17]. The friction resulting from the mutual interaction is typically discussed in the context of translational motion. Here, different friction regimes are identified depending on the center-of-mass velocity. In the low-speed regime ($v \ll 1000$ cm/s) [18], the system is close to equilibrium and friction is governed by Brownian motion, in which the stochastic behavior is dominant. In the high-speed regime [17,18], the system is strongly out of equilibrium and the friction force is proportional to the number

of collisions with surface corrugations per unit time [17], and thus the friction becomes viscous.

Compared to friction in translational motion, the case of purely rotational friction has received less attention. Since high-tangential-velocity (outer) and low-tangential-velocity (inner) atoms are present at the same time and both sets are forced to move concurrently, the extent to which the results for translational friction can be applied in a purely rotational setting is not obvious. In this context, rotating gears are of particular interest for the miniaturization of mechanical devices. They are key components of many potential applications, such as the implementation of nanoscale analog computing devices (analogous to the Pascaline [19]) or in nanorobotics [20].

Over recent years, gears have been successfully downsized to the nanoscale. The miniaturization has been achieved through bottom-up approaches by synthesizing molecular gears [21], and through top-down methods, such as focused-ion-beam [22] or electron-beam [23,24] techniques, which allow etching solid-state gears. For molecule gears, many issues, such as motor effects [25–29], manipulation [30–33], and transmission [34–36], have been studied. For solid-state gears, a recent study has focused on transmission of rotational motion in gear trains [36].

In this work, we focus on diamond-based solid-state gears rotating on a substrate (see Fig. 1). We use various combinations of gears and substrate materials to address the associated questions about the dependence of rotational friction on the crystal structure of the substrate and the gear size. For this type of problem, it is suitable to use classical

*hhlin@nano.tu-dresden.de

†<https://nano.tu-dresden.de/>

molecular-dynamics (MD) simulations as in previous studies of translational friction [17,18]. This approach allows us to take a large number of atoms into account and, moreover, to reach relevant time scales [37] in the range of 100 ps up to 1 ns.

The paper is organized as follows. In Sec. II, we introduce the setup of the gear-substrate system and also the technical details of the MD simulations. In Sec. III, we study a diamond-based solid-state gear on a SiO_2 substrate with given initial angular velocity and investigate its slowing down. This is followed by a study of dissipation with different combinations of gear sizes and substrate materials. Then, we investigate various setups involving different degrees of conformational freedom of the gear-plus-substrate system to explore its influence on friction. Furthermore, we study the effect of the thickness of the substrate and the resulting phonon excitation by using kinetic energy spectra. This shows that the low-frequency surface phonon is excited during the gear rotation.

II. MODEL SYSTEM AND COMPUTATIONAL APPROACH

In this section, we introduce the system setup and provide details on the MD simulations.

A. Setup

To start our study of how energy can be dissipated from the gear into the surface, we consider the system shown in Fig. 1. Here, we put a diamond-based solid-state gear with radius $r = 5$ nm and thickness 9.8 Å (with 8544 carbon atoms) on top of a SiO_2 (001) surface [see Fig. 2(a)]. The geometry of the solid-state gear is created on the basis of the general algorithm for involute [38] spur gears [39], which can be implemented by using the Open Visualization Tool (OVITO) [40] to cut the gear from a bulk diamond crystal. For the substrate, we create

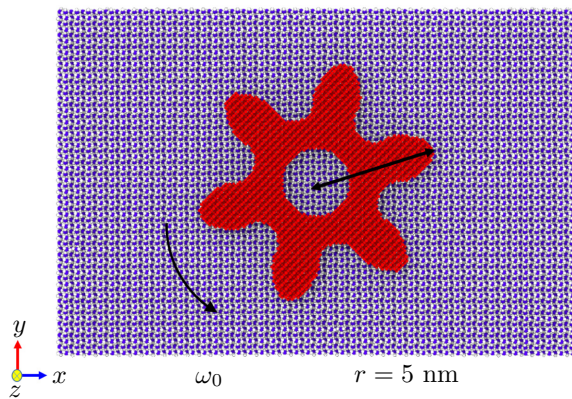


FIG. 1. A schematic illustration of a diamond-based solid-state gear with radius $r = 5$ nm rotating with angular velocity ω_0 on top of a α -cristobalite SiO_2 (001) substrate.

an α -cristobalite SiO_2 (001) surface (with size 23.0 nm \times 15.3 nm \times 1.39 nm, which contains 32 400 atoms) from Visual Molecular Dynamics (VMD) [41] with periodic boundary conditions in the x and y directions. We then combine the gear and substrate together with an initial vertical separation of 2.5 Å. To prevent lateral and vertical motion, we fix the bottom layer of the substrate (with thickness 3 Å) and allow the remaining part (a region with thickness 11 Å) to relax. Then, a geometry optimization is performed using the conjugate gradient method within the MD simulation software, which will be discussed in detail later.

To compare different materials, we prepare the system with the same diamond gear but with two different substrate materials: amorphous SiO_2 and graphene [see Figs. 2(b) and 2(c)]. For the amorphous SiO_2 , we create a substrate with dimension 28.2 nm \times 16.9 nm \times 1.86 nm and set the initial vertical separation to be approximately 1 to 2 Å (since the surface has many asperity points, the distance is not well defined). To prevent net translation of the substrate, we fix the bottom layer with a thickness 5.8 Å to mimic the semi-infinite bulk material. Then, we allow only the remaining layer with a thickness of 12.8 Å to be relaxed. For graphene, the substrate size is 21.8 nm \times 12.6 nm \times four monolayers, with an initial vertical separation of 2 Å. The bottom monolayer is kept fixed and the other three layers are allowed to relax.

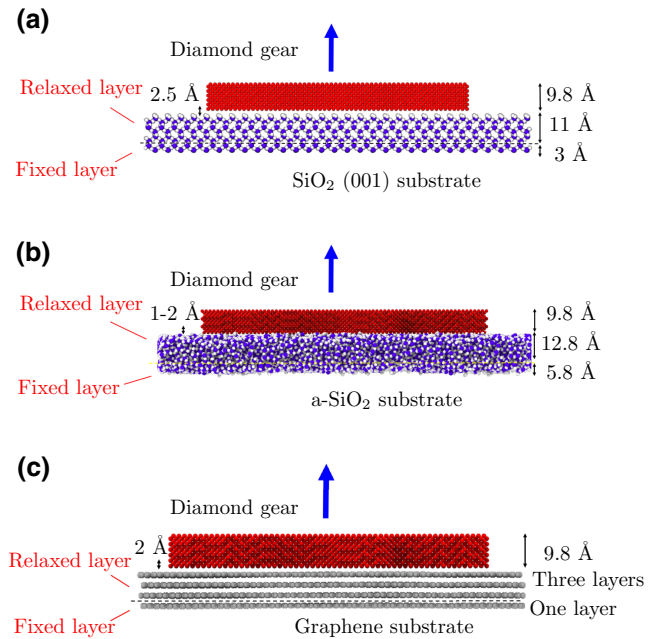


FIG. 2. The scheme of the 5-nm diamond-based solid-state gear on top of the (a) α -cristobalite SiO_2 with size 23.0 nm \times 15.3 nm \times 1.39 nm and separation distance 2.5 Å, (b) amorphous SiO_2 with dimension 28.2 nm \times 16.9 nm \times 1.86 nm and separation distance around 1 – 2 Å, and (c) four-layer graphene with size 21.8 nm \times 12.6 nm \times four monolayers and separation distance 2 Å.

B. Molecular dynamics

Once the system is set up, the next step is to define the simulation protocol for the MD. Here, we use the Large-scale Atomic/Molecular Massively Parallel Simulator (LAMMPS) [42] for implementing the MD simulations.

For the force fields, we choose the Tersoff potential [43] inside the SiO₂ substrate. Inside diamond, we use the adaptive intermolecular reactive empirical bond order (AIREBO) potential [44], which is an established bond-order potential specifically developed to describe allotropes of carbon. Between the gear and substrate, we specify a 12–6 type Lennard-Jones potential $V_{LJ}(r)$:

$$V_{LJ}(r) = 4\epsilon \left[\left(\frac{\sigma}{r} \right)^{12} - \left(\frac{\sigma}{r} \right)^6 \right], \quad (1)$$

where r is the interatomic distance. Here, we choose the LJ parameters [45]: $\epsilon_{C-Si} = 8.91$ meV, $\epsilon_{C-O} = 3.44$ meV and $\sigma_{C-Si} = 3.629$ Å, $\sigma_{C-O} = 3.275$ Å. Note that between the diamond gear and the graphene substrate, the van der Waals interaction is automatically included in the AIREBO potential among carbon atoms [44]. To fix the rotation axle, we attach a spring with a high spring constant $k = 1.6 \times 10^4$ N/m (1000 eV/Å²) to the gear center of mass and we fix the temperature $T = 10$ K with the substrate subject to the canonical ensemble implemented by the Nosé-Hover thermostat [46,47].

III. RESULTS

In this section, we investigate the friction process by considering the relaxation of the angular velocity via pure Lennard-Jones interactions between gear and substrate. We then address the issue of how different combinations of gear sizes and substrate materials affect the friction. To investigate the dissipation channels in the system, we restrict the dynamics to rigid-body motion for the gear and the substrate for several different cases: rigid gear with a deformable substrate, a rigid substrate with deformable gear, and both rigid. Finally, we study the influence of the thickness of the substrate relaxed layer and compute the corresponding kinetic energy spectra.

A. Viscous dissipation and rotational motion

Considering that the atoms inside a rotating gear are moving with higher tangential velocity on average, we may expect that the rotational friction still corresponds to the high-tangential-velocity friction regime as found for translational motion [17]. Accordingly, a gear with instantaneous angular velocity ω is subject to a nonconservative torque equal to $-\gamma\omega$:

$$I\dot{\omega} = -\gamma\omega, \quad (2)$$

where γ is the damping coefficient and I is the gear moment of inertia. Therefore, in a first step, we give an

initial angular velocity to the gear (which rotates with respect to a fixed center of mass) and check if this viscous dissipation law will emerge as a result of van der Waals interactions between the gear and the substrate at fixed temperature. To be specific, we set several different initial angular velocities $\omega_0 = 0.1, 0.15,$ and 0.2 rad/ps and then let the system relax over 100 ps. In Fig. 3(a), the velocity relaxation of a rotating gear due to the interaction with the substrate is shown. One can see that the frictional behavior agrees with the viscous damping rather well, which can be further seen from the plot of the normalized angular velocity in Fig. 3(b). Additionally, the angular-velocity relaxation for the gear weakly depends on the initial velocity, except for a small fluctuation in the case of $\omega_0 = 0.1$ rad/ps (there is a kink around 65 ps due to the internal deformation). We can extract the corresponding relaxation time τ using the region from 0 to 50 ps (highlighted in yellow), by fitting the curve to the exponential function $\propto e^{-t/\tau}$ [dashed lines in Fig. 3(a)], which gives the relaxation times 58.62, 54.55, and 56.22 ps

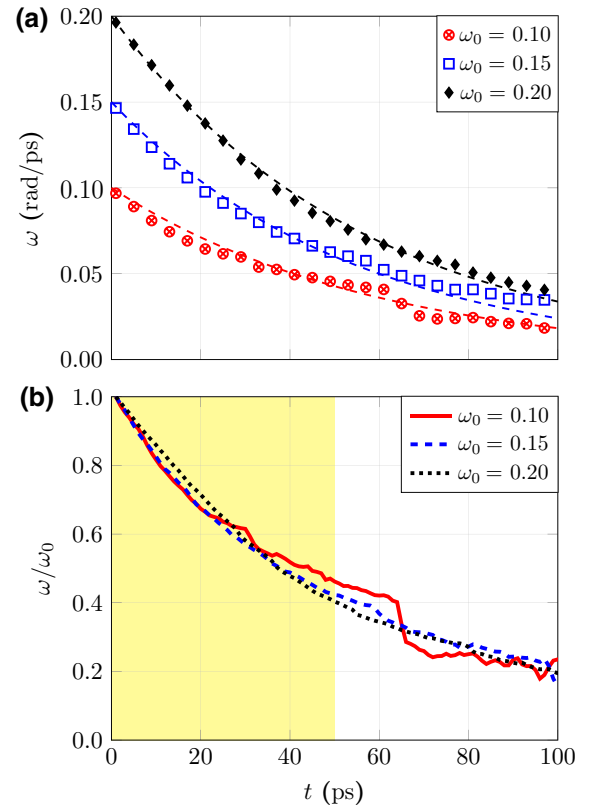


FIG. 3. The (a) angular velocity (exponential fits indicated by dashed lines) and (b) normalized angular velocity of the 5-nm diamond gear on top of α -cristobalite SiO₂ undergoing a relaxation within the simulation time $t = 100$ ps with different initial angular velocities $\omega = 0.1, 0.15,$ and 0.2 rad/ps, respectively. The highlighted yellow region (from 0 to 50 ps) is used for extracting the velocity relaxation time τ by fitting to an exponential function $\propto e^{-t/\tau}$.

for $\omega_0 = 0.1, 0.15$, and 0.2 rad/ps, respectively. Note that the relaxation time is related to the damping coefficient γ through the relation $\tau = I/\gamma$. Another observation is that the gear with size $r = 5$ nm behaves like a deterministic rotor instead of a Brownian rotor, since the stochastic behavior is suppressed with increasing gear size. This implies that the friction of the 5-nm involute shape gear is in the high-average-tangential-velocity dissipation regime.

B. Effect of substrate material and gear size

Apart from the gear on top of the crystalline SiO_2 substrate, one may ask how different combinations of gear and substrate would affect the friction. To avoid too many variables, we use diamond gears and gradually reduce their size. For the substrate, we change the material from α -cristobalite SiO_2 to amorphous SiO_2 and finally to a few layers of graphene, as shown in Fig. 2.

With the above setup, we perform a 100-ps MD simulation at temperature $T = 10$ K with the initial angular velocity $\omega_0 = 0.2$ rad/ps. The results are shown in Fig. 4. We change the gear radius from 5 nm to 3 nm for crystalline SiO_2 (α -cristobalite), amorphous SiO_2 , and graphene in Figs. 4(a)–4(c), respectively. One can see that as the gear size reduces to 3 nm (black dotted line), the gear motion becomes fluctuating, especially for amorphous SiO_2 and graphene. This is related to the fact that when the rotational kinetic energy becomes smaller, the gear will be more sensitive to surface vibrations, which are determined by $k_B T$ and, therefore, the gear starts entering the low-average-tangential-velocity dissipation regime, in which Brownian behavior becomes dominant. Next, we extract the corresponding relaxation times from the curves and summarize them in Table I. One can clearly see that for crystalline SiO_2 , the relaxation times are approximately independent of the gear size. However, the relaxation time for amorphous SiO_2 shows that as the gear size reduces, the relaxation becomes much shorter. For graphene, the relaxation time is around 70 ps and is independent of gear size. Compared to SiO_2 , the graphene substrate is essentially flat on the length scale of the gear. Thus, the coupling between the gear and the substrate is less effective in this case. Based on our simulations, amorphous SiO_2 shows the largest friction coefficient, crystalline SiO_2 has an intermediate value, and graphene shows the smallest friction coefficient.

C. Dissipation and available degrees of freedom

Although the dissipation is directly related to the interaction with the substrate, the detailed mechanism for the energy transfer is still unclear. Therefore, in this section, we discuss how the different number of available degrees of freedom can affect the dissipation. Here, we will discuss four different cases: case 1, gear and substrate both rigid bodies; case 2, deformable gear and rigid substrate; case

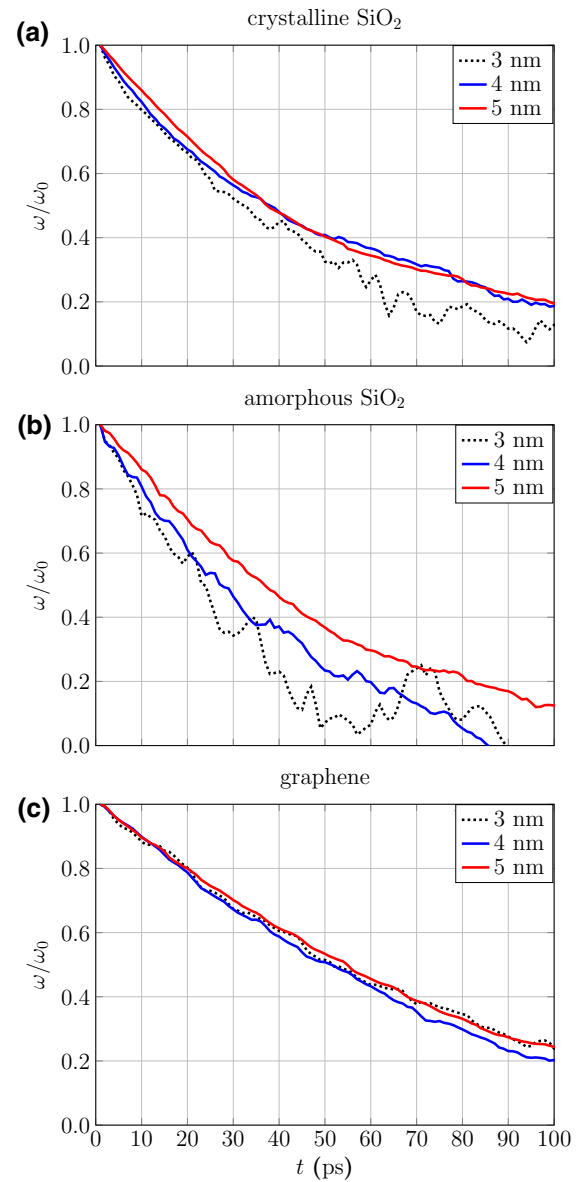


FIG. 4. The normalized angular velocity of the diamond-based solid-state gear with initial angular velocity $\omega_0 = 0.2$ rad/s for different gear radii $r = 3, 4$, and 5 nm on top of (a) crystalline SiO_2 , (b) amorphous SiO_2 , and (c) four-layer graphene, respectively.

3, rigid gear and deformable substrate; and case 4, both gear and substrate deformable. Case 1 is trivial as long as the gear motion is still a planar rotation, since the rotating gear will move in a potential-energy surface, which is defined collectively by the atoms in the frozen substrate. Therefore, the gear will keep rotating or oscillating permanently without any dissipation. In case 2, the gear is allowed to deform but the substrate is frozen. Therefore, the potential-energy surface is still the same as in case 1. However, the rotating gear can now also transfer energy to the internal degrees of freedom of the gear, leading to

TABLE I. The moments of inertia I (in units of 10^{-40} kg m²) and angular-velocity relaxation times in units of picoseconds for different combinations of gear size and substrate material. The corresponding damping coefficients γ in units of 10^{-30} kg/ps are given in parentheses.

Size	3 nm	4 nm	5 nm
I	1.98	6.22	19.7
c-SiO ₂	46.87 (4.22)	53.09 (11.72)	56.22 (34.86)
a-SiO ₂	29.92 (6.62)	39.25 (15.85)	54.20 (36.16)
Graphene	75.17 (2.63)	69.76 (8.92)	76.22 (25.71)

a deformation of the gear. For case 3, the gear is rigid but the substrate is deformable. Therefore, the potential-energy surface is no longer well defined and the force acting on the gear is not conservative, since the energy can be transported away from the surface by bulk phonons. However, if the angular velocity of the gear is sufficiently high, it will experience a force resulting from the averaged motion of the surface. Finally, case 4 is a mixture of cases 2 and 3, which has two dissipation channels at the same time. The results of cases 2–4 are shown in Fig. 5. We compare the angular-velocity relaxation among different cases and materials with the same initial angular velocity $\omega = 0.2$ rad/ps, gear radius $r = 5$ nm, and temperature $T = 10$ K (if the substrate is deformable) within 100 ps. One can see that the angular-velocity relaxation corresponding to the deformable gear and substrate is faster than that of the rigid gear or rigid substrate, which provides strong evidence that the whole dissipation channel is composed of channel 1 (gear deformation) and channel 2 (surface vibration), which is independent of substrate material (except for the small angular-velocity regime of amorphous SiO₂ substrate due to the location of asperity points). Also, channel 2 dissipates more efficiently than channel 1, which implies that surface vibrations are more important than gear deformation for the substrates considered in this study.

D. Thickness dependence and surface-phonon excitation

Since we find that the dissipation is mainly coming from surface vibrations, it is interesting to see how the dissipation can gradually emerge when the thickness of the relaxed layer in Fig. 2 is changed. Note that the overall thickness of the substrate in the simulations is always the same and that only the thickness of the fixed layer is changed. The results for crystalline SiO₂ are shown in Fig. 6(a). One can see that as the thickness d of the relaxed layer increases, the angular-velocity relaxation time τ becomes shorter. However, the thickness dependence is only important when d is not too large. As one can see, when d approaches 14 Å, the decay rate starts to saturate.

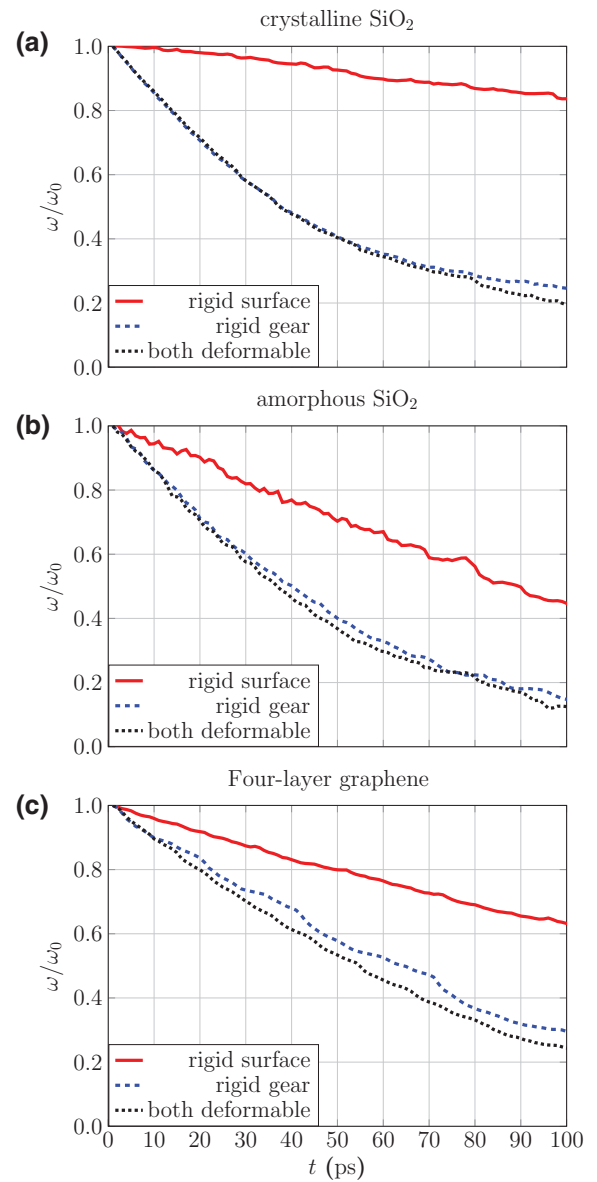


FIG. 5. The normalized angular velocity with initial angular velocity $\omega = 0.2$ rad/ps for different cases of the available degrees of freedom—rigid surface, rigid gear, and both deformable—for (a) crystalline SiO₂, (b) amorphous SiO₂, and (c) graphene.

To gain additional insight, we define the kinetic energy spectrum $K(\nu)$ [48,49] given by

$$K(\nu) = \sum_{i \in R} K_i(\nu) = \sum_{i \in R} \frac{1}{2} m_i |\mathbf{v}_i(\nu)|^2, \quad (3)$$

where $\mathbf{v}_i(\nu)$ is the Fourier transform of the velocity of the i th atom in the relaxed layer (R) and ν is the frequency. To identify the features arising purely from rotational dissipation, we show the kinetic energy spectra for the cases without and with gear rotation. The use of a time step of

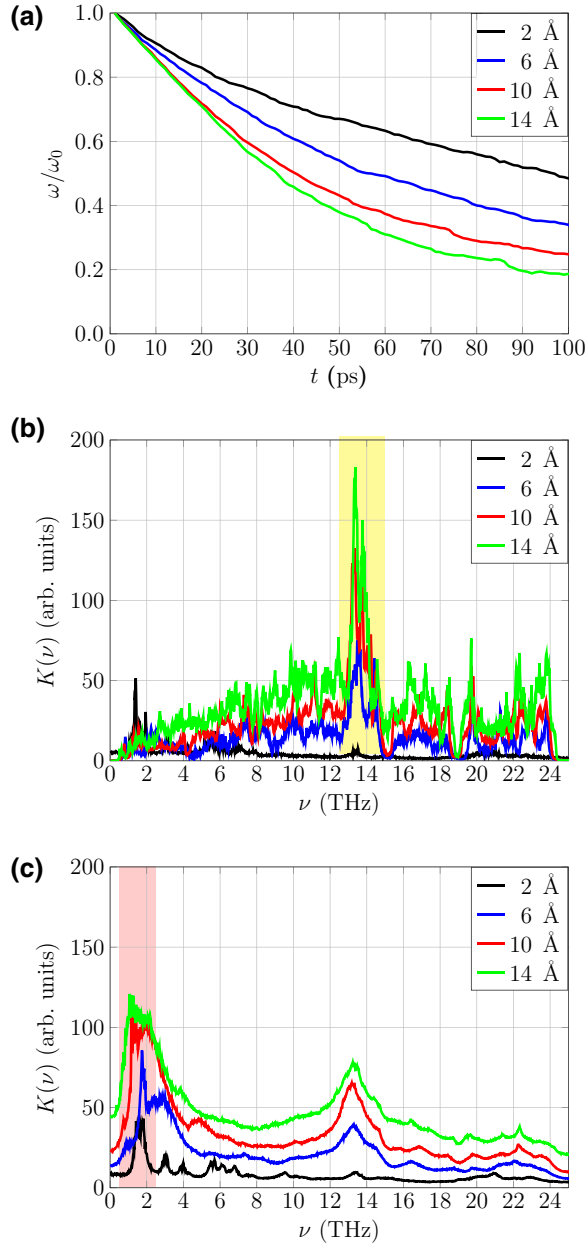


FIG. 6. (a) The relaxed-layer thickness dependence of the angular-velocity relaxation. (b,c) Kinetic energy spectra of the substrate (b) without and (c) with gear rotation within 50 ps.

20 fs and a total simulation time of 50 ps gives a maximal frequency equal to 25 THz and a resolution of 0.02 THz for the spectra. The results are shown in Figs. 6(b) and 6(c), respectively. In Fig. 6(b), one can see that as the thickness increases, a feature around 13 THz appears. This feature can be associated with the van Hove singularity of the phonon density of states for the crystalline SiO₂ thin film. Without gear rotation, the system is in a state of thermal equilibrium for which the equipartition theorem

applies and one finds that [48,49]

$$\rho(\nu) \propto \frac{K(\nu)}{\frac{3}{2}N_R k_B T}, \quad (4)$$

where $\rho(\nu)$ is the phonon density of states (PDOS) and N_R is the number of atoms in the relaxed layer. Moreover, k_B denotes the Boltzmann constant and T is the temperature. The peak position at 13 THz also agrees with the PDOS from density-functional perturbation theory (DFPT) calculations [50].

Now, we can compare the kinetic energy spectrum with that during the first 50 ps shown in the yellow region in Fig. 3(b), which is the duration of the dissipation process. The result is shown in Fig. 6(c). One can see that when the gear is rotating and dissipating energy, the original peak at 13 THz is broadened, which means that the lifetime of this vibrational mode becomes shorter. At the same time, the gear also excites low-frequency modes around 1–2 THz, which can be estimated by using the harmonic approximation of the Lennard-Jones interaction between Si-O and C atoms with corresponding frequencies $\nu_{\text{Si}} = 1.83$ and $\nu_{\text{O}} = 2.42$ THz. Moreover, the amplitude of the spectrum increases as the thickness becomes larger, which indicates that more energy has been dissipated into the substrate and phonons are excited. However, the thickness effect becomes less important since the amplitudes do not change too much as the thickness gets larger than 10 Å. This implies that only surface phonons are excited, which is also consistent with our previous finding for the angular-velocity relaxation in Fig. 6(a).

E. Phonon mode visualization

To better understand the excited modes before and during the gear rotation, we filter the kinetic energy spectrum for a given frequency ν_0 . In order to do this, we apply a band filter to the kinetic energy spectrum for the i th atom as follows:

$$K_i(\nu_0) = \int_{-\infty}^{\infty} K_i(\nu) \mathcal{W}(\nu - \nu_0) d\nu. \quad (5)$$

In practical terms, we use a rectangular window function:

$$\mathcal{W}(\nu - \nu_0) \approx \frac{\theta[\nu - (\nu_0 - \Gamma/2)] - \theta[\nu - (\nu_0 + \Gamma/2)]}{\Gamma}, \quad (6)$$

where Γ is the bandwidth of the window around ν_0 and the function $\theta(\nu)$ is the step function. The respective windows are highlighted in Figs. 6(b) and 6(c). The features around 2 and 13 THz are of particular interest. Therefore, we compare the corresponding modes at these frequencies before and during gear rotation for the crystalline SiO₂ substrate with a relaxed-layer thickness of 14 Å, which corresponds

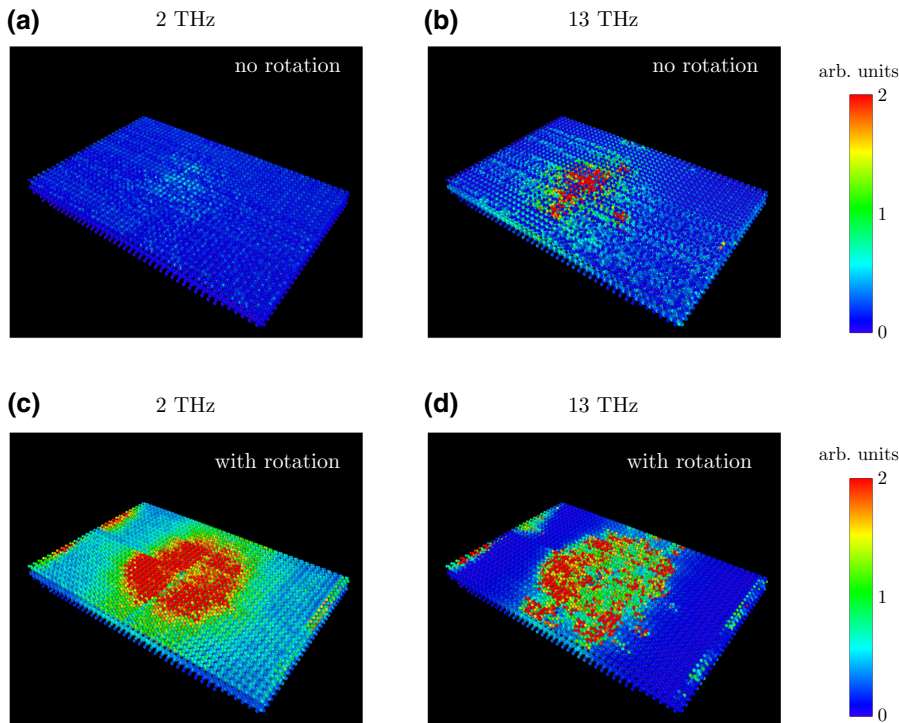


FIG. 7. The three-dimensional topography of the intensity from the kinetic energy spectrum $K_j(\nu_0)$ with a contribution around the following frequencies (with bandwidth $\Gamma = 1$ THz): (a) $\nu = 2$ THz without rotation, (b) $\nu = 13$ THz without rotation, (c) $\nu = 2$ THz during rotation, and (d) $\nu = 13$ THz during rotation.

to the green line in Fig. 6. The resulting distributions in real space are shown in Fig. 7 for a bandwidth $\Gamma = 1$ THz. From the top view, one can see that without gear rotation there are more atoms excited at 13 THz than at 2 THz, which is consistent with the features found in Fig. 6(b). To further see in detail how the mode is distributed in the z direction, we plot the average of the kinetic energy spectrum $K_i(\nu_0)$ by spatially binning in the z direction with $N_{\text{bin}} = 7$ bins. Note that $z = 0$ is at the bottom of the crystalline SiO_2 slab. The results are shown in Fig. 8. The blue and red dashed lines represent the results for 2 THz and 13 THz before the gear rotation, respectively. For 13 THz, there is a plateau between $z = 3$ Å and $z = 9$ Å, which means that this mode resembles a bulk normal mode as expected. As for 2 THz, the intensity is everywhere very low compared to 13 THz, since no mode has been excited yet.

Similarly, we repeat the procedure for the case with gear rotation. As shown in Figs. 7(c) and 7(d), the mode at 2 THz is strongly excited and localizes below the gear (the red region around the center), which is also consistent with the spectra in Fig. 6. However, for 13 THz, there is also a visible pattern, which is apparently due to the gear rotation. To gain more insight, we show the resulting distribution in the z direction in Fig. 8. The blue and red solid lines are the results during the gear rotation. For 2 THz (the blue solid line), the mode is strongly excited for $z > 10$ Å. This implies that this mode behaves like a surface phonon. As for 13 THz (the red solid line), the intensity in the middle of the slab is reduced compared to the case without

gear rotation, which is also consistent with the difference between the peak heights observed in Figs. 6(b) and 6(c) at 13 THz. On the surface ($z > 10$ Å), however, the intensity is enhanced due to the gear rotation. Therefore, this situation corresponds to a mixture of bulk phonons and surface phonons.

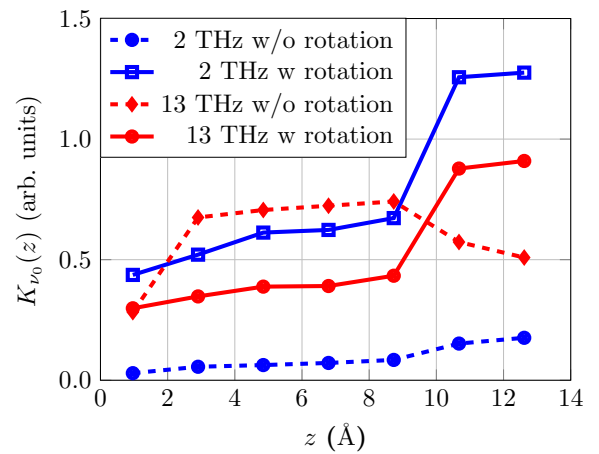


FIG. 8. The vertical distribution of the average kinetic energy spectrum $K_{\nu_0}(z)$ of the substrate with the relaxed-layer thickness 14 Å, where z is the position relative to the bottom of the crystalline SiO_2 substrate. The blue and red lines show $K_{\nu_0}(z)$ for $\nu_0 = 2$, and $\nu_0 = 13$ THz, respectively; the dashed line and solid line represent $K_{\nu_0}(z)$ before and during the gear rotation, respectively.

IV. CONCLUSION AND OUTLOOK

In this study, we show that viscous dissipation can emerge from pure van der Waals interactions between gears and substrates. The corresponding angular-velocity relaxation time can be extracted by fitting the results from the MD simulation to an exponential decay. We also study the effect of different gear sizes and substrate materials. The results show that the relaxation time decreases monotonically as the gear size reduces for amorphous SiO₂ but it weakly depends on the size for crystalline SiO₂ and graphene. Concerning the substrate, amorphous SiO₂ gives the largest friction coefficient, crystalline SiO₂ has an intermediate value, and graphene shows the smallest friction coefficient. Then, we investigate the effect of different cases with varying degrees of structural flexibility (different numbers of degrees of freedom) in both the gear and the substrate, and find that the dissipation process is composed of different channels involving gear deformations and surface vibrations, respectively. The latter are found to be more important than gear deformations. Finally, we find that the dissipation depends on the thickness of the substrate and also directly relates to the excitation of low-frequency vibrational surface modes. For the example of SiO₂, we find a surface-phonon mode at 2 THz to be dominant.

Future studies will need to address frictional processes at even smaller scales, involving molecule gears on metal substrates [4,51]. In this situation, dissipation channels involving electronic degrees of freedom become highly relevant, so that computationally more expensive force fields, such as reactive force fields (like ReaxFF) [52], will be required to perform MD simulations for such systems. Finally, we hope that atomistic studies combined with further developments of the necessary fabrication tools will provide the possibility to fine tune the design of solid-state gears at the nanometer scale.

ACKNOWLEDGMENTS

We thank A. Kutscher, J. Heinze, S. Kampmann, D. Bodesheim, N. Lorente, C. Joachim, and F. Moresco for useful discussions and suggestions. This work has been supported by the International Max Planck Research School (IMPRS) for “Many-Particle Systems in Structured Environments” and also by the European Union Horizon 2020 FET Open Project “Mechanics with Molecules” (MEMO, Grant No. 766864). We also acknowledge the Center for Information Services and High Performance Computing (ZIH) at TU Dresden for computational resources.

[1] K. M. Sankar, D. Kakkar, S. Dubey, S. V. Garimella, M. Goyat, S. Joshi, and J. K. Pandey, Theoretical and

- computational studies on nanofriction: A review, *Proc. Inst. Mech. Eng. Part J J. Eng. Tribol.* **234**, 448 (2020).
- [2] A. Vanossi, N. Manini, M. Urbakh, S. Zapperi, and E. Tosatti, Colloquium: Modeling friction: From nanoscale to mesoscale, *Rev. Mod. Phys.* **85**, 529 (2013).
- [3] E. Gnecco and E. Mayer, *Fundamentals of Friction and Wear*, edited by E. Gnecco and E. Meyer, NanoScience and Technology (Springer, Berlin, Heidelberg, 2007).
- [4] B. Persson and E. Tosatti, *Physics of Sliding Friction*, edited by B. N. J. Persson and E. Tosatti (Springer, Netherlands, Dordrecht, 1996), Vol. 311.
- [5] S. Wen and P. Huang, *Principles of Tribology* (John Wiley & Sons Singapore Pte. Ltd., Singapore, 2017).
- [6] N. Manini, O. M. Braun, E. Tosatti, R. Guerra, and A. Vanossi, Friction and nonlinear dynamics, *J. Phys. Condens. Matter* **28**, 293001 (2016).
- [7] G. Tomlinson, CVI. A molecular theory of friction, *London, Edinburgh, Dublin Philos. Mag. J. Sci.* **7**, 905 (1929).
- [8] O. M. Braun and Y. S. Kivshar, *The Frenkel-Kontorova Model* (Springer, Berlin, Heidelberg, 2004).
- [9] E. Panizon, G. E. Santoro, E. Tosatti, G. Riva, and N. Manini, Analytic understanding and control of dynamical friction, *Phys. Rev. B* **97**, 104104 (2018).
- [10] M. S. Lodge, C. Tang, B. T. Blue, W. A. Hubbard, A. Martini, B. D. Dawson, and M. Ishigami, Lubricity of gold nanocrystals on graphene measured using quartz crystal microbalance, *Sci. Rep.* **6**, 31837 (2016).
- [11] E. D. Smith, M. O. Robbins, and M. Cieplak, Friction on adsorbed monolayers, *Phys. Rev. B* **54**, 8252 (1996).
- [12] M. Walker, C. Jaye, J. Krim, and M. W. Cole, Frictional temperature rise in a sliding physisorbed monolayer of Kr/graphene, *J. Phys. Condens. Matter* **24**, 424201 (2012).
- [13] G. Binnig, C. F. Quate, and C. Gerber, Atomic Force Microscope, *Phys. Rev. Lett.* **56**, 930 (1986).
- [14] G. Binnig, H. Rohrer, C. Gerber, and E. Weibel, Tunneling through a controllable vacuum gap, *Appl. Phys. Lett.* **40**, 178 (1982).
- [15] G. Binnig and H. Rohrer, Scanning tunneling microscopy—From birth to adolescence, *Rev. Mod. Phys.* **59**, 615 (1987).
- [16] S. G. Balakrishna, A. S. de Wijn, and R. Bennewitz, Preferential sliding directions on graphite, *Phys. Rev. B* **89**, 245440 (2014).
- [17] R. Guerra, U. Tartaglino, A. Vanossi, and E. Tosatti, Ballistic nanofriction, *Nat. Mater.* **9**, 634 (2010).
- [18] M. S. Tomassone, J. B. Sokoloff, A. Widom, and J. Krim, Dominance of Phonon Friction for a Xenon Film on a Silver (111) Surface, *Phys. Rev. Lett.* **79**, 4798 (1997).
- [19] D. Roegel, A mechanical calculator for arithmetic sequences (1844–1852): Part 1, historical context and structure, *IEEE Ann. Hist. Comput.* **37**, 90 (2015).
- [20] D. P. Sierra, N. A. Weir, J. Jones, and Frank, Sandia Rep., Tech. Rep. October, Sandia National Laboratories (SNL), Albuquerque, NM, and Livermore, CA, 2005.
- [21] Y. Gisbert, S. Abid, G. Bertrand, N. Saffon-Merceron, C. Kammerer, and G. Rapenne, Modular synthesis of pentaaryl cyclopentadienyl Ru-based molecular machines via sequential Pd-catalysed cross couplings, *Chem. Commun.* **55**, 14689 (2019).

- [22] Y. Ju Yun, C. Seong Ah, S. Kim, W. Soo Yun, B. Chon Park, and D. Han Ha, Manipulation of freestanding Au nanogears using an atomic force microscope, *Nanotechnology* **18**, 505304 (2007).
- [23] J. Deng, C. Troadec, F. Ample, and C. Joachim, Fabrication and manipulation of solid-state SiO₂ nano-gears on a gold surface, *Nanotechnology* **22**, 275307 (2011).
- [24] J. Yang, J. Deng, C. Troadec, T. Ondarçuhu, and C. Joachim, Solid-state SiO₂ nano-gears AFM tip manipulation on HOPG, *Nanotechnology* **25**, 465305 (2014).
- [25] H. H. Lin, A. Croy, R. Gutierrez, C. Joachim, and G. Cuniberti, Current-induced rotations of molecular gears, *J. Phys. Commun.* **3**, 025011 (2019).
- [26] J. Echeverria, S. Monturet, and C. Joachim, One-way rotation of a molecule-rotor driven by a shot noise, *Nanoscale* **6**, 2793 (2014).
- [27] A. Croy and A. Eisfeld, Dynamics of a nanoscale rotor driven by single-electron tunneling, *EPL (Europhys. Lett.)* **98**, 68004 (2012).
- [28] S. Stolz, O. Gröning, J. Prinz, H. Brune, and R. Widmer, Molecular motor crossing the frontier of classical to quantum tunneling motion, *Proc. Natl. Acad. Sci.* **117**, 14838 (2020).
- [29] I. A. Pshenichnyuk and M. Čížek, Motor effect in electron transport through a molecular junction with torsional vibrations, *Phys. Rev. B* **83**, 165446 (2011).
- [30] F. Eisenhut, J. Meyer, J. Krüger, R. Ohmann, G. Cuniberti, and F. Moresco, Inducing the controlled rotation of single o-MeO-DMBI molecules anchored on Au(111), *Surf. Sci.* **678**, 177 (2018).
- [31] C. Manzano, W.-H. Soe, H. S. Wong, F. Ample, A. Gourdon, N. Chandrasekhar, and C. Joachim, Step-by-step rotation of a molecule-gear mounted on an atomic-scale axis, *Nat. Mater.* **8**, 576 (2009).
- [32] N. Koumura, R. W. J. Zijlstra, R. A. van Delden, N. Harada, and B. L. Feringa, Light-driven monodirectional molecular rotor, *Nature* **401**, 152 (1999).
- [33] Y. Zhang, J. P. Calupitan, T. Rojas, R. Tumbleson, G. Erbland, C. Kammerer, T. M. Ajayi, S. Wang, L. A. Curtiss, A. T. Ngo, S. E. Ulloa, G. Rapenne, and S. W. Hla, A chiral molecular propeller designed for unidirectional rotations on a surface, *Nat. Commun.* **10**, 3742 (2019).
- [34] H.-H. Lin, A. Croy, R. Gutierrez, C. Joachim, and G. Cuniberti, Mechanical Transmission of Rotational Motion between Molecular-Scale Gears, *Phys. Rev. Appl.* **13**, 034024 (2020).
- [35] W.-H. Soe, S. Srivastava, and C. Joachim, Train of single molecule-gears, *J. Phys. Chem. Lett.* **10**, 6462 (2019).
- [36] H.-H. Lin, J. Heinze, A. Croy, R. Gutierrez, and G. Cuniberti, in *Build. Probing Small Mech.* (Springer, Nature Switzerland AG, 2020), Chap. 11, p. 165.
- [37] B. Persson and A. Nitzan, Linear sliding friction: On the origin of the microscopic friction for Xe on silver, *Surf. Sci.* **367**, 261 (1996).
- [38] The involute shape was proposed by Euler as an optimized geometry for classical rigid-body transmission.
- [39] R. L. Norton, *Machine Design: An Integrated Approach* (Prentice Hall, Upper Saddle River, 2010), 4th ed.
- [40] A. Stukowski, Visualization and analysis of atomistic simulation data with OVITO—The Open Visualization Tool, *Model. Simul. Mater. Sci. Eng.* **18**, 015012 (2010).
- [41] W. Humphrey, A. Dalke, and K. Schulten, VMD: Visual molecular dynamics, *J. Mol. Graph.* **14**, 33 (1996).
- [42] S. Plimpton, Fast parallel algorithms for short-range molecular dynamics, *J. Comput. Phys.* **117**, 1 (1995).
- [43] J. Tersoff, New empirical approach for the structure and energy of covalent systems, *Phys. Rev. B* **37**, 6991 (1988).
- [44] S. J. Stuart, A. B. Tutein, and J. A. Harrison, A reactive potential for hydrocarbons with intermolecular interactions, *J. Chem. Phys.* **112**, 6472 (2000).
- [45] N. Inui and S. Iwasaki, Interaction energy between graphene and a silicon substrate using pairwise summation of the Lennard-Jones potential, *e-J. Surf. Sci. Nanotechnol.* **15**, 40 (2017).
- [46] S. Nosé, A unified formulation of the constant temperature molecular dynamics methods, *J. Chem. Phys.* **81**, 511 (1984).
- [47] W. G. Hoover, Canonical dynamics: Equilibrium phase-space distributions, *Phys. Rev. A* **31**, 1695 (1985).
- [48] S. V. Meshkov, Low-frequency dynamics of Lennard-Jones glasses, *Phys. Rev. B* **55**, 12113 (1997).
- [49] C. Lee, D. Vanderbilt, K. Laasonen, R. Car, and M. Parrinello, *Ab initio* studies on the structural and dynamical properties of ice, *Phys. Rev. B* **47**, 4863 (1993).
- [50] B. Wehinger, A. Bosak, K. Refson, A. Mirone, A. Chumakov, and M. Krisch, Lattice dynamics of α -cristobalite and the boson peak in silica glass, *J. Phys. Condens. Matter* **27**, 305401 (2015).
- [51] M. S. Tomassone and A. Widom, Electronic friction forces on molecules moving near metals, *Phys. Rev. B* **56**, 4938 (1997).
- [52] K. Chenoweth, A. C. T. van Duin, and W. A. Goddard, ReaxFF reactive force field for molecular dynamics simulations of hydrocarbon oxidation, *J. Phys. Chem. A* **112**, 1040 (2008).